Ilias Bosdas
Laboratory for Energy Conversion,
Department of Mechanical
and Process Engineering,
ETH Zurich,
Zurich 8092, Switzerland
e-mail: bosdas@lec.mavt.ethz.ch

Michel Mansour
Laboratory for Energy Conversion,
Department of Mechanical
and Process Engineering,
ETH Zurich,
Zurich 8092, Switzerland
e-mail: michel.mansour@lec.mavt.ethz.ch

Anestis I. Kalfas
Department of Mechanical Engineering,
Aristotle University of Thessaloniki,
Thessaloniki 54124, Greece
e-mail: akalfas@auth.gr

Reza S. Abhari
Laboratory for Energy Conversion,
Department of Mechanical
and Process Engineering,
ETH Zurich,
Zurich 8092, Switzerland
e-mail: rabhari@lec.mavt.ethz.ch

Shigeki Senoo
Mitsubishi Hitachi Power Systems, Ltd.,
3-1-1, Saiwai,
Hitachi 317-0073, Ibaraki, Japan
e-mail: shigeki1_senoo@mhps.com

Unsteady Wet Steam Flow Field Measurements in the Last Stage of Low Pressure Steam Turbine

Modern steam turbines need to operate efficiently and safely over a wide range of operating conditions. This paper presents a unique unprecedented set of time-resolved steam flowfield measurements from the exit of the last two stages of a low pressure (LP) steam turbine under various volumetric massflow conditions. The measurements were performed in the steam turbine test facility in Hitachi city in Japan. A newly developed fast response probe equipped with a heated tip to operate in wet steam flows was used. The probe tip is heated through an active control system using a miniature high-power cartridge heater developed in-house. Three different operating points (OPs), including two reduced massflow conditions, are compared and a detailed analysis of the unsteady flow structures under various blade loads and wetness mass fractions is presented. The measurements show that at the exit of the second to last stage the flow field is highly three dimensional. The measurements also show that the secondary flow structures at the tip region (shroud leakage and tip passage vortices) are the predominant sources of unsteadiness at 85% span. The high massflow operating condition exhibits the highest level of periodical total pressure fluctuation compared to the reduced massflow conditions at the inlet of the last stage. In contrast at the exit of the last stage, the reduced massflow operating condition exhibits the largest aerodynamic losses near the tip. This is due to the onset of the ventilation process at the exit of the LP steam turbine. This phenomenon results in three times larger levels of relative total pressure unsteadiness at 93% span, compared to the high massflow condition. This implies that at low volumetric flow conditions the blades will be subjected to higher dynamic load fluctuations at the tip region.
[DOI: 10.1115/1.4031345]

Introduction

Due to the increasing share of renewable power within the existing electrical power network, industrial steam turbines require operational flexibility. They need to be efficiently operated over a wide range of operating conditions at different mass flow rates and with different exit vacuum pressures. In order to achieve an effective increase in power output, the annulus area of the last stage is continuously being increased [1]. The last two stages of the LP section are critical segments of large-scale steam turbines. The aerodynamic design of these stages of the machine has a direct impact on their mechanical robustness; knowing that the unsteady blade loading leading to high cycle fatigue of the rotating components is directly coupled to the evolution of the unsteady three-dimensional flowfield. However, there is a lack of time-resolved experimental data measured in the wet steam environment of the last two stages of LP steam turbines.

Five-hole probes equipped with an air purging system are commonly used in the wet steam environment of the last two stages of the LP steam turbines. However, they are no longer suitable to study and quantify the unsteady blade row interactions affecting the aeromechanical performance of the axial-flow turbomachines [2,3]. So far, experimental studies of the unsteady aerodynamic excitation of LP steam blade have been conducted in down-scaled air models as reported in Ref. [4].

On the other hand, recent advances in the computational fluid dynamics (CFD) models enable numerical studies simulating unsteady three-dimensional wet steam flows through multistage LP turbine models as reported in Refs. [5–9]. Nevertheless, the lack of unsteady experimental data constrains the validation of the codes to measurements conducted in cascades in wind tunnels [6] or to time-averaged pressure measurements performed in a wet steam environment of large steam turbines, as presented in Refs. [10–13]. Yet, more accurate predictions are achieved when the measured unsteady flow field can be used for validation. In that regard, Shibukawa et al. [14] investigated the vibration stress behavior and the unsteady pressures under flash back conditions in a subscale steam turbine test model, using fast response pressure sensors mounted on turbine's wall and rotating blades. Their results show that there is a correlation between an unsteady flow field and the blade excitation modes. Segawa et al. [15] used flush mounted pressure transducers in order to study the flow field under various operating conditions in a four-stage LP steam turbine. The pressure sensors were mounted on the turbine sidewalls and on the stators' surface. The same study reported that pressure fluctuations become larger with decreased volumetric flow at the outer and inner sidewalls and this phenomenon follows the same tendency of the blade dynamic stress characteristics. As far as the authors are aware, there have been only few attempts to perform time-resolved flowfield measurements in the last two stages of LP steam turbines. Gerschütz et al. [16] manufactured a fast response total pressure probe for measurements in wet steam. Two different kinds of probes were used in these measurements. Both probes consist of two pneumatic pressure taps for balancing in flow direction and one total pressure tap equipped with Kulite sensor for

unsteady total pressure measurements. The probes can operate up to 275 °C and have a tip diameter of 6 mm. A detailed fast Fourier transform (FFT) analysis is described in their results upstream of the last stage, downstream of the stator, and at the exit of the last stage of a scaled steam turbine test facility. Their study presents the importance of the unsteady flow interactions with the rotating blades. The results have shown unsteady flow instabilities arising from the tip leakage flow that rotate at the circumferential direction together with the rotor rotational speed.

This paper presents time-resolved relative flow angle and total pressure measurements at the rotor exit of the last two stages of an LP steam turbine. The measurements were conducted with a newly developed miniature fast-response aerodynamic heated probe, which can be used in wet steam flows with wetness mass fractions of up to 15%. The probe's robustness and ability to provide high-frequency bandwidth measurements in wet steam turbine flows is demonstrated in measurements conducted at MHPS' (Mitsubishi Hitachi Power Systems) research steam turbine test facility under various operating conditions. In a second step, the evolution of the unsteady relative total pressure distribution across the span at the exit of the rotor is studied in detail for various massflow conditions.

FRAP High Temperature Heated Probe

The design and operation of the current fast-response aerodynamic probe is based on the developments made over the past two decades at the laboratory for Energy Conversion at ETH Zürich [17–20]. Similarly to the probe developed by Lenherr et al. [19], the fast response aerodynamic probe–high temperature heated (FRAP-HTH) has two piezo-resistive sensors encapsulated into a probe tip diameter of 2.5 mm which can be operated up to a temperature of 500 K.

In order to maximize the output power of large steam turbines, the enthalpy difference between the inlet and exit of the machine has to be kept as high as possible. Therefore, the steam is expanded below saturation conditions and the last two stages operate under wet steam flow conditions. In order to operate the probe with unclogged pressure taps, the probe tip is heated a couple of degrees above the flow saturation temperature T_{sat}, as shown in Table 1. It should be noted that the FRAP-HTH is equipped with shielded pressure taps protecting the miniature piezo resistive sensors from direct water particle impacts. The FRAP-HTH probe design and operating principle is described in more detail in Ref. [21].

As shown in Fig. 2, the probe tip is heated using an in-house miniature high power density heater located in close vicinity to the tip. The temperature of the probe tip is controlled using a proportional-integral-derivative (PID) controller regulator. In order to ensure the highest absolute measurement accuracy, the probe tip is kept at a constant temperature at each measurement traverse. The tip temperature is equal to

$$T_{tip} = T_{sat} + \Delta T \qquad (1)$$

The tip temperature is regulated using the temperature output of either the yaw or the pitch pressure sensor membrane T_{yaw} and T_{pitch} as an input to the PID regulator. The PID regulator adjusts the feeding current across the heater until the target temperature is reached.

The high signal-to-noise ratio enables measurements of ± 25 Pa in the last stages of the machine where the absolute pressure levels are below 10% of the ambient pressure.

Virtual Six Sensor Measurement Concept. Due to large flare angles present in the LP steam turbines, the FRAP-HTH is calibrated and operated in a virtual six-sensor mode as depicted in Fig. 3. The virtual six sensor measurement concept is an extension of the virtual four-sensor concept described in Refs. [18] and [19].
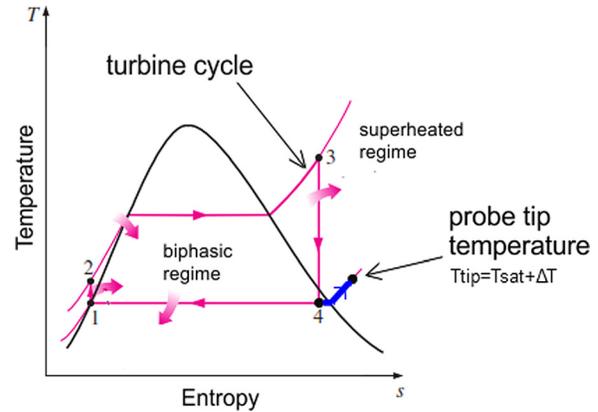
Fig. 1 T–S diagram with steam turbine operating cycle and the respective probe tip operating temperature

The schematic in Fig. 3 shows the measurement concept in a virtual six sensor mode with a two-sensor probe (two pressure taps).

The first sensor, located behind pressure tap 1, is used to measure the actual tap pressures (p1, p2, p3) in three consecutive steps. It evaluates the three different probe set angles (0 deg, −42 deg, +42 deg) relative to the probe stem. The second sensor, which is located behind pressure tap 2, is used for the fourth pressure (p4) at the roll set angle equal to 0 deg, and p5 and p6 pressures are measured at −42 deg and +42 deg roll angles, respectively. Out of this procedure, a set of six independent pressures (p1–p6) is obtained. These pressure values are then used for the definition of the different flow coefficients for flow yaw and pitch angles, static and total pressure as well as the Mach number, as shown in Table 1.

As defined in Table 1, two sets of aerodynamic calibration coefficients are defined depending on the magnitude of the pitch incidence angle relative to the probe tip. This choice is made according to the measured pressure value of the two sensors as shown in Fig. 4. When the measured pressure value of the yaw sensor P1 is higher than the pressure value P4 of the pitch sensor, the probe is operated using the calibration coefficients defined for sector 1. For this new probe shape geometry, the condition is fulfilled at Ma = 0.3, when the flow pitch angle is ≤ 26 deg for the yaw incidence angle of 0 deg relative to the probe, the change of the coefficients at the edges of the yaw angle calibration range occurs at 22 deg pitch. For this case, the aerodynamic coefficients are standard as described in Refs. [18] and [19] and summarized in Table 1. A second set of aerodynamic coefficients is used for high pitch flow angles (sector 2, Fig. 4) when the pressure value P4 of the pitch sensor is higher than the pressure value P1 of the yaw sensor.

In the postprocessing code, each pressure data sample is checked independently. The first set of aerodynamic coefficients is used when P1 ≥ P4 (sector 1) is fulfilled in order to derive the yaw, pitch, total pressure, and static pressure and the second set of coefficients is used when P1 < P4 (sector 2).

Aerodynamic Probe Calibration. The aerocalibration of the probe tip was performed in the fully automated freejet facility at ETH Zürich. The probe is installed on a three-axis traversing system in order to rotate the probe relative to the fixed jet. The automatic calibration procedure follows a predefined measurement grid for different probe yaw and pitch angles. The set of calibration data is taken on a homogenous grid that covers ±26 deg in yaw angle and −5 deg to 49 deg in pitch angle. The spatial distribution of the calibration coefficients for the two sectors is presented in detail in Ref. [21].

The polynomial curve-fit method of Gallington [22] is applied to the calibration data. The derived calibration model accuracy is given in Table 2 for the flow angle range of interest. The model

Table 1 Extended aerodynamic calibration coefficients for the FRAP-HTH probe

Coefficients when $P_1 \geq P_4$ sector 1 (blue sector)	Coefficients when $P_4 > P_1$ sector 2 (red sector)
$K_\phi = \dfrac{P_2 - P_3}{P_1 - \dfrac{(P_2 + P_3)}{2}}$	$K_\phi = \dfrac{P_5 - P_6}{P_4 - \dfrac{(P_5 + P_6)}{2}}$
$K_\gamma = \dfrac{P_1 - P_4}{P_1 - \dfrac{(P_2 + P_3)}{2}}$	$K_\gamma = \dfrac{P_4 - P_1}{P_4 - \dfrac{(P_5 + P_6)}{2}}$
$K_t = \dfrac{P_{tot} - P_1}{P_1 - \dfrac{(P_2 + P_3)}{2}}$	$K_t = \dfrac{P_{tot} - P_4}{P_4 - \dfrac{(P_5 + P_6)}{2}}$
$K_s = \dfrac{P_{tot} - P_{stat}}{P_1 - \dfrac{(P_2 + P_3)}{2}}$	$K_s = \dfrac{P_{tot} - P_{stat}}{P_4 - \dfrac{(P_5 + P_6)}{2}}$

A. Probe tip (Diameter: 2.5mm)
B. Heating elements (Diameter: 4.7mm)
C. Heater temperature monitoring (T_{heater})
D. Tip temperature monitoring (T_{tip})
E. 8mm shaft
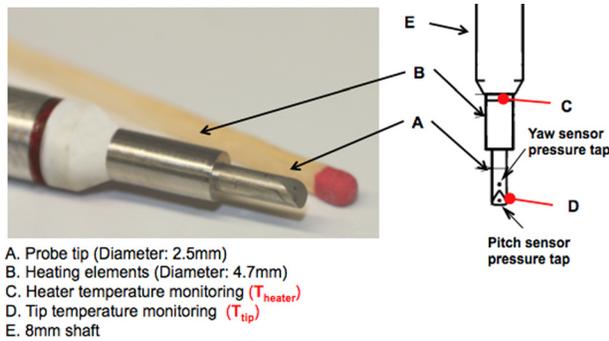
Fig. 2 FRAP-HT heated probe schematic and temperature measurement locations

accuracy is given in absolute values for the flow angles, as well as for total and static pressure. The accuracy for the Mach number is given as a percentage of the freejet calibration Mach number. Additionally, for total and static pressure, the accuracy is presented as a percentage of the real dynamic head at the freejet Mach number of 0.5.

Uncertainty Analysis. Similar to the analysis conducted by Behr et al. [23], the whole chain of uncertainty sources has been accounted for. It includes the uncertainties resulting from the calibration references and the polynomial interpolation curves of the
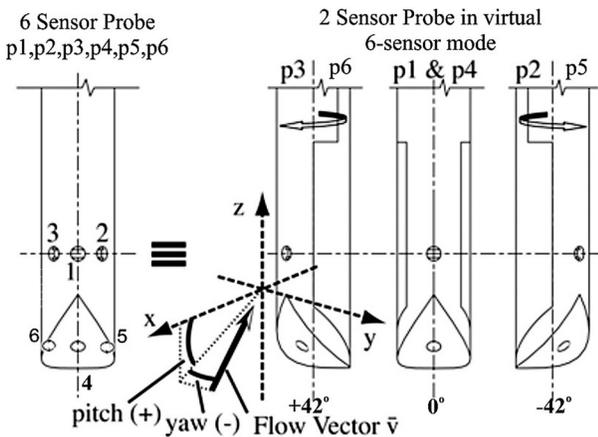
Fig. 3 Measurement concept in virtual six-hole mode with two-hole probe
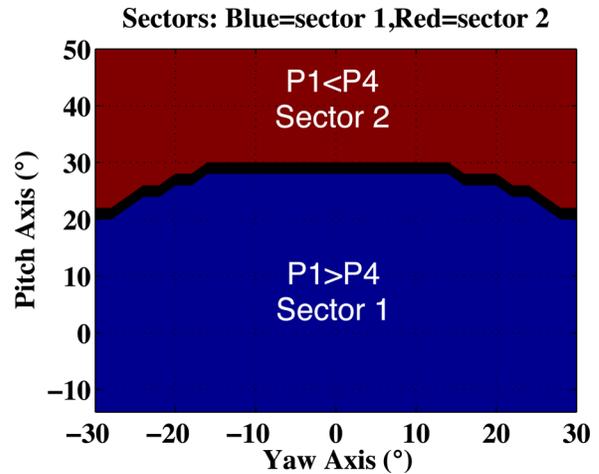
Fig. 4 FRAP-HTH extended calibration section's schematic for Ma = 0.3

Table 2 FRAP-HTH calibration model accuracy for Ma = 0.5 and calibration range of ±26 deg in yaw and −5 deg < pitch < 49 deg in pitch

Parameter	Probe accuracy	
	Sector 1	Sector 2
φ	0.15 deg	0.11 deg
γ	0.37 deg	0.07 deg
P_{tot}	122 Pa (0.66%P_{dyn})	38 Pa (0.21%P_{dyn})
P_{stat}	177 Pa (0.97%P_{dyn})	103 Pa (0.57%P_{dyn})

calibration models, as well as the uncertainty sources related to the measurements. The resulting overall uncertainties are calculated using the Gaussian error propagation formula. The uncertainty calculation was performed using the Guide to the expression of Uncertainty in Measurement (GUM) Workbench. Table 3 summarizes the respective measurement error for the current average measurement conditions. The relative total pressure coefficient is defined in the below equation:

$$\mathrm{Cpt_{rel}} = \frac{P_{t,rel,FRAP-HTH} - P_{s,exit}}{P_{t,inlet} - P_{s,exit}} \qquad (2)$$

Effect of Probe Heating on Measured Flow Quantities. In order to investigate the potential effect of the heater and the heated tip on the potential flow field around the probe, tests were conducted under representative flow conditions of the last stage of the LP steam turbine in Freejet facility, prior to the measurement campaign. The results have shown that the heater which leads to an overheat of the probe tip has no effect on the measured flow quantities. The streamlines of the flow at the measurement

Table 3 FRAP-HTH uncertainty calculated for L-0 stage at OP-3 of steam turbine test facility

Parameter	Uncertainty
φ	±0.30 deg
γ	±0.43 deg
P_{tot}	±150 Pa (1.4% P_{tot})
P_{stat}	±210 Pa (2.2% P_{stat})
Ma	±0.07
Ma_{rel}	±0.04
φ_{rel}	±1.8 deg
Cpt_{rel}	±0.071

location are not deviated and therefore the flow angles as well as the total and static pressures are not affected. The measurement tests were conducted under representative Nusselt number conditions of the last stage of the MHPS' steam test facility and resulted in a Mach number of 0.17. Different overheat ratios above the flow temperature were tested. For an overheat of $\Delta T = 10$ K, the deviation on all calibration coefficients is below 0.5%. In order to provide a magnitude on resulted flow parameters, measurements were taken with the heater activated and deactivated at different yaw and pitch angles in Freejet facility. The resulted difference on the measured yaw and pitch angles is, on average, below 0.03 deg and 0.07 deg, respectively, and for total and static pressures below 10 Pa and 30 Pa, respectively. This results in errors that are within the uncertainty of the aerocalibration model as presented in Table 2 and practically proves that the effect of the heater has no impact on the measured aerodynamic flow quantities. Further results for different Mach numbers and overheat ratios are presented in Ref. [21].

Experimental Facility

All measurements were conducted at the MHPS research steam turbine test facility for thermal power generation in Hitachi city, Japan. As shown in Fig. 5, the experimental test facility is a four stage (L-3 to L-0) LP steam turbine with a scale ratio of 1/2.2. The steam is generated in the boiler and then guided to the inlet of the turbine through a control valve. The inlet pressure and temperature can be adjusted in order to change the OP, and therefore, the loading conditions of the machine. Downstream of the last stage of the turbine the steam condensates and returns back to the boiler to complete the cycle. An orifice flowmeter and flow nozzle are installed in order to measure the mass flow in the main steam pipe and the condensation pipe, respectively. A generator and a water break absorb the turbine's power and control the rotational speed of the machine. The rated speed of the machine is 7920 rpm. The three different operating conditions tested in this measurement campaign are summarized in Table 4.

The measurement planes of the current experimental work are presented in Fig. 6. All measurements were performed at the exit of the L-1 and L-0 stages downstream of the rotor. The number of the rotor blades is 96 and 70 for L-1 and L-0, respectively. Both stages are equipped with a part-span connector (PSC) located at 52% and 50% span at L-1 and L-0 rotor blades, respectively. The PSC is elliptical snubber, which is integrally manufactured with the blade. It has an elliptical cylinder shape with fillets on the blade. The data are acquired at a sampling rate of 200 kHz over a period of 2 s with a resolution of 24 bit. The postprocessing is done for three consecutive rotor pitches. The sampling rate resolves 16 points in the rotor relative frame of reference. The probe was mounted on a two-axis

Table 4   Operating tested conditions

		OP-3	OP-2	OP-1
Massflow (t/h)		67	52	52
Exit pressure (kPa)		8.0	8.0	10.7
Inlet temperature (°C)		266	266	266
Wetness mass fraction (%)	L-1	3.1	2.5	2.3
	L-0	8.0	6.5	4.5

traversing system enabling a single traverse at each plane from blade hub to blade tip with the possibility of rotation around its stem axis. The spatial resolution of the measurement grid at the traverse planes consisted of 33 and 31 radial points for L-1 and L-0 planes, respectively, and all points were equal.

Results and Discussion

Time-Averaged Measurement Comparison. The FRAP-HTH time-averaged measurements are now compared to 5HP (pneumatic five-hole probe) measurements conducted on the same day at L-1 and L-0 stages' exit. The 5HP consists of a typical cobra shape probe with a tip diameter of 5 mm and is equipped with a standard air purging system. The FRAP-HTH and the 5HP measurements were performed along a single radial traverse, and it should be noted that the 5HP access hole is located at a different upstream stator clocking position compared to the FRAP-HTH. The 5HP measurements were performed with a radial spatial resolution of 33 mm. The FRAP-HTH measurements are time-averaged over 80 rotor revolutions for three rotor blade passing events. The two sets of measurements are compared at L-0 and L-1 rotor exit for operating condition OP-3, which exhibits the most severe conditions with an average wetness mass fraction of 8.0% and 3.1% at L-0 and L-1, respectively.

Time-Averaged Results Comparison at L-1 Rotor Exit. Figure 7 shows the FRAP-HTH and the 5HP relative yaw flow angle as well as the absolute Mach number across the blade span at L-1 rotor exit. There is good overall agreement between the two probes, both in the trend and in absolute values across the span. Both probes capture the two peaks of local flow overturning located at 58% and 45% span, which are generated by the presence of the PSC at 52%. The effect of the PSC can also be seen in Fig. 7(b), where the FRAP-HTH measurements show two clear local peaks of absolute Mach number. They occur at 58% and 45% span, and are caused by the blockage generated by the PSC. The RMS (root mean square) value of the yaw angle difference is 2.8 deg and 0.03 in the absolute Mach number. It is believed that the offset in the measured relative yaw angle is in part due to probe alignment error during installation.

Fig. 5   LP steam turbine test facility where FRAP-HTH measurements were conducted
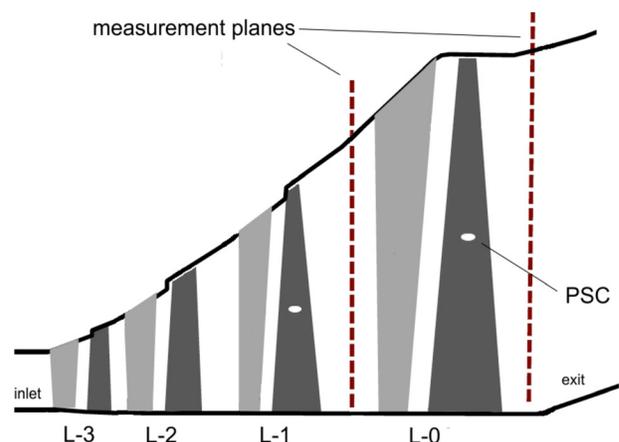
Fig. 6   Schematic of the steam turbine test facility with the respective probe measurement locations
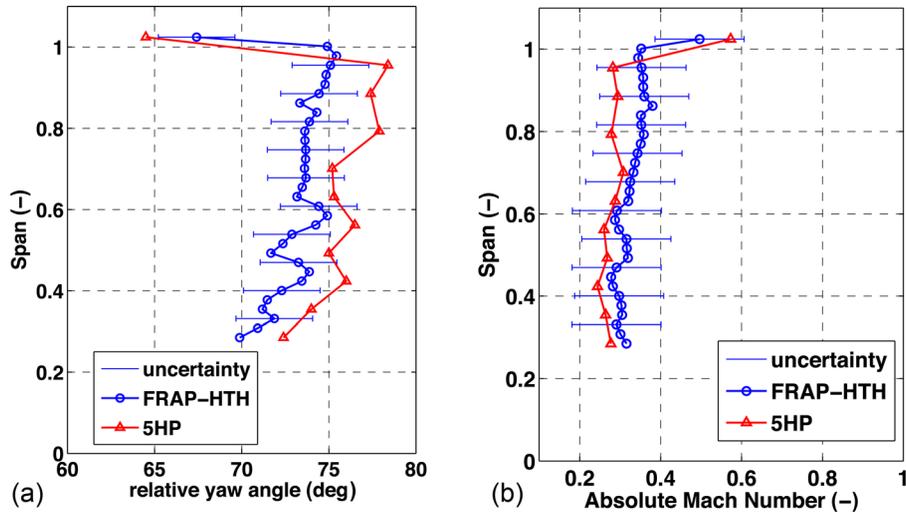
Fig. 7 Relative flow yaw angle (*a*) and absolute Mach number (*b*) measured by the 5HP and FRAP-HTH probes at rotor exit of L-1 stage
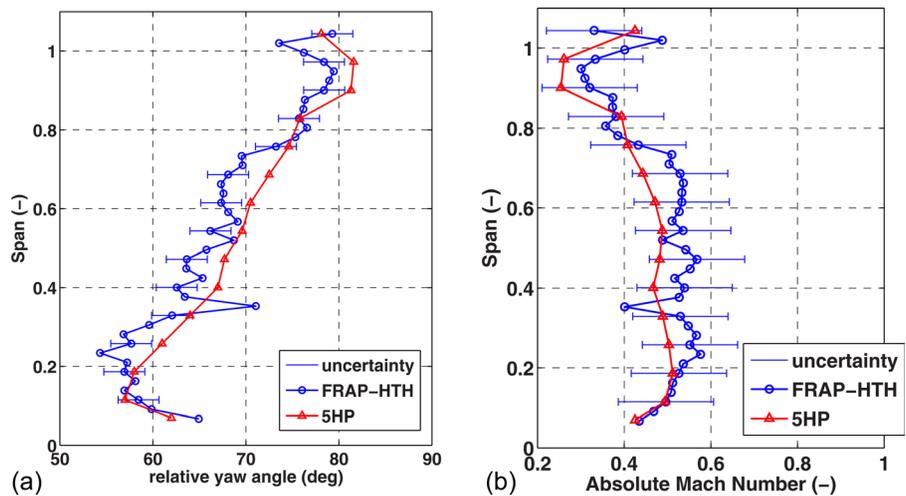
Fig. 8 Relative flow yaw angle (*a*) and absolute Mach number (*b*) of 5HP and FRAP-HTH probes at rotor exit of L-0 stage

Time-Averaged Results Comparison at L-0 Rotor Exit. Figure 8 shows the FRAP-HTH and the 5HP measured relative yaw flow angle as well as the absolute Mach number across the blade span at the L-0 rotor exit.

In general, there is a good agreement between the two probes, both in the trend and in absolute values. As shown in Fig. 8(*a*), both probes capture the overturning centered at 95% span related to the presence of the tip secondary flow structures. Unlike the 5HP measurements, the denser FRAP-HTH radial measurement grid allows us to capture two peaks of local flow overturning at 57% and 35% span, which are generated by the presence of the PSC located at 50%, as reported in Ref. [8]. The effect of the PSC can also be seen in Fig. 8(*b*), where the FRAP-HTH measurements show two local peaks of absolute Mach number, at 52% and 35% span, due to the redistribution of the flow around the PSC. The RMS value of the relative yaw angle difference between the FRAP-HTH and 5HP measurements is 1.6 deg and 0.1 for the absolute Mach number. These measured deviations are within both probes' measurement uncertainty bandwidth. This is despite the fact that both probes have different radial measurement spacing and are located at different upstream stator clocking position.

These results demonstrate the ability of the newly developed FRAP-HTH probe to provide reliable flow angle and Mach number measurements at the last two stages of LP steam turbines under elevated wetness flow conditions.

Steady Flow Field at Rotor Exit of L-1 Stage. In this paragraph, the time-averaged FRAP-HTH measurement results at the rotor exit of L-1 stage are presented for the three different operating conditions listed in Table 4. All plots show measurement results from 1.03 down to 0.3 span. Figure 9(*a*) shows the spanwise distribution of the time-averaged total pressure coefficients, as defined in Eq. (2), in the rotor relative frame of reference. In the same graphs, the maximum and minimum values obtained from the time-resolved data are plotted as well. OP-3 has on an average a 2% deficit in the mean value of the Cpt_{rel} across the whole span compared to the other two conditions. On the other hand, OP-1 and OP-2 demonstrate very similar Cpt_{rel} distribution.

In order to analyze the flowfield further, the blade span was subdivided in four main regions. These are the hub region from 0.28 to 0.4 span; the midspan region containing the snubber interface from 0.4 to 0.6 span; the tip region from 0.6 to 1 span; and finally the shroud region up to 1.03 span. Equation (3) is used to compare the magnitude of the periodical fluctuations along the

blade span between the three measured operating conditions. For each span location i, the difference of the peak-to-peak fluctuations is divided by the averaged $\overline{Cpt}_{rel}$ value. Table 5 summarizes the results for OP-1, OP-2, and OP-3.

$$\left.\frac{\widetilde{Cpt}_{rel,max} - \widetilde{Cpt}_{rel,min}}{\overline{Cpt}_{rel}} \times 100\%\right|_{span(i)} \tag{3}$$
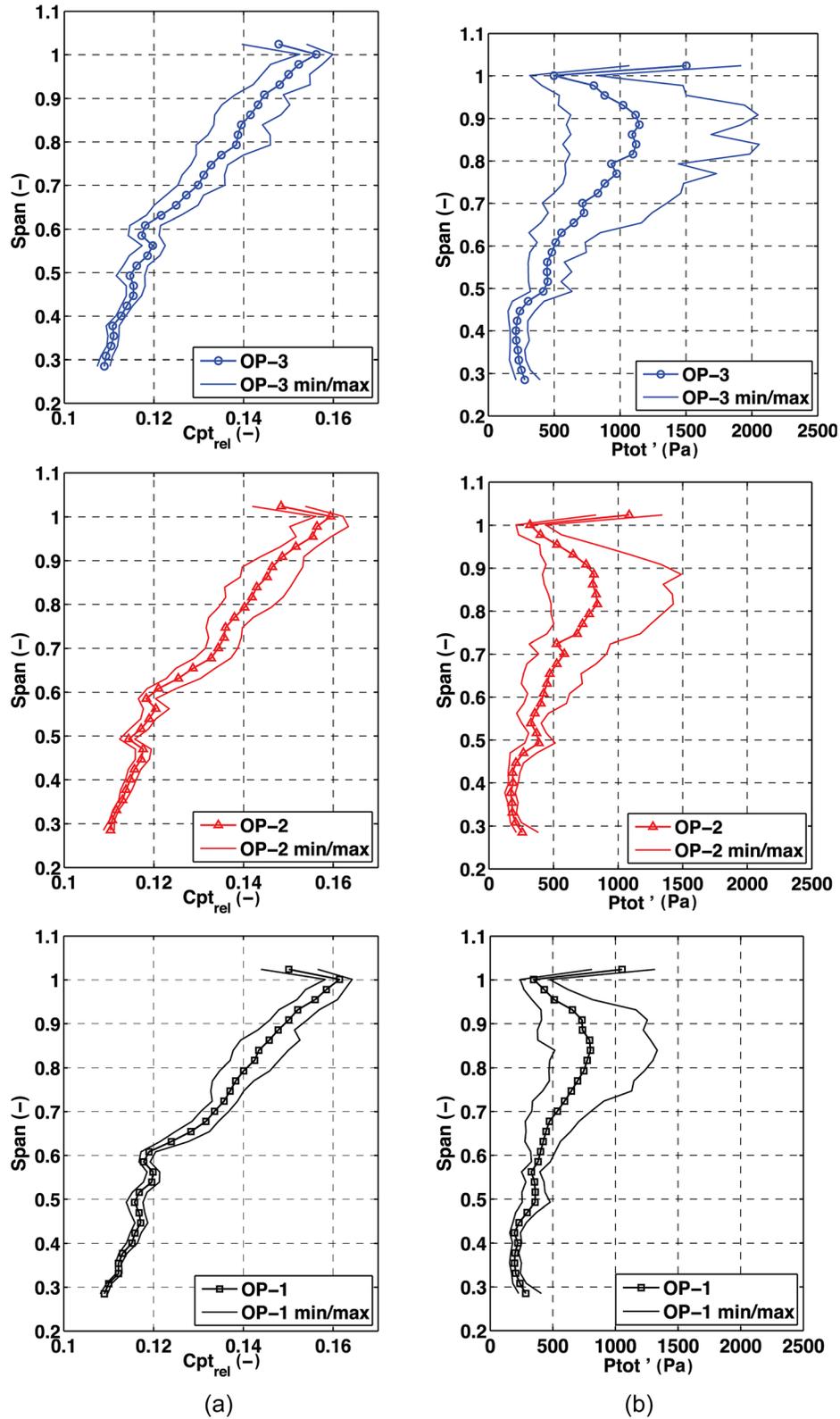
Fig. 9 (a) Time-averaged spanwise distribution of Cpt_{rel} and (b) time-averaged RMS of P'_{tot} (Pa) at rotor exit of L-1 stage for OP-3, OP-2 and OP-1 with their respective minimum and maximum values obtained from the time-resolved data

Table 5 Spanwise distribution of peak to peak fluctuation of Cpt$_{rel}$ as a function of the local mean value for OP-1, OP-2, and OP-3 conditions

Region	Span (%)	OP-1 (%)	OP-2 (%)	OP-3 (%)
Hub	28–40	1.3	1.6	2.4
Midspan	40–60	2.5	3.1	4.1
Tip	60–98	5.9	6.9	8.1
Shroud	98–103	5.9	6.7	7.4

As seen in Table 5, all conditions experience the highest Cpt$_{rel}$ variation at the tip and shroud locations with gradually decreasing levels of fluctuations until the hub region. OP-3 shows the highest amplitude of unsteady fluctuations at all spanwise locations compared to OP-2 and OP-1. In the tip region OP-3 shows periodical fluctuations in Cpt$_{rel}$, which are 37% and 14.8% higher than for OP-1 and OP2, respectively. At the midspan location between 40 and 60% span, the variation in Cpt$_{rel}$ is found to be higher in OP-3 by 64% and 32% compared to OP-1 and OP-2, respectively, which signifies more intense flow interactions with the PSC for the high massflow operating condition. In the shroud region, the labyrinth leakage flow also generates losses that strongly depend on the operating condition and it will be shown in the subsequent paragraphs that the stochastic unsteadiness is also maximized at that location for this measurement plane. Finally at the hub section between 28 and 40% span, OP-3 condition demonstrates 2.4% peak to peak oscillations of the mean value, which is still 85% greater compared to OP-1 and 50% higher compared to OP-2.

The averaged aerodynamic losses are triggered by unsteady secondary flow structures. As Porreca et al. [24] described, the RMS value of the random part of the pressure signal acquired with the FRAP-HTH, as defined in Eq. (4), has shown to be an appropriate indicator to identify regions of elevated aerodynamic losses. Based on the triple decomposition of the time-resolved pressure signal, the random part of the signal can be calculated as the difference between the raw pressure signal $p(t)$ of the FRAP-HTH probe and the phase-locked averaged one $(\bar{P}_{(t)} + \tilde{P}_{(t)})$, as depicted in the below equation:

$$P'_{(t)} = P_{(t),FRAP} - (\bar{P}_{(t)} + \tilde{P}_{(t)}) \tag{4}$$

Figure 9(b) shows the time-averaged distribution RMS of P'_{tot}, for OP-1, 2, and 3 with their respective maximum and minimum values resulting from the time-resolved measurements. In all cases, the tip region of the blade span exhibits the highest levels of RMS of P'_{tot} and Cpt$_{rel}$ values. This observation is in good agreement in location and in the order of magnitude of the
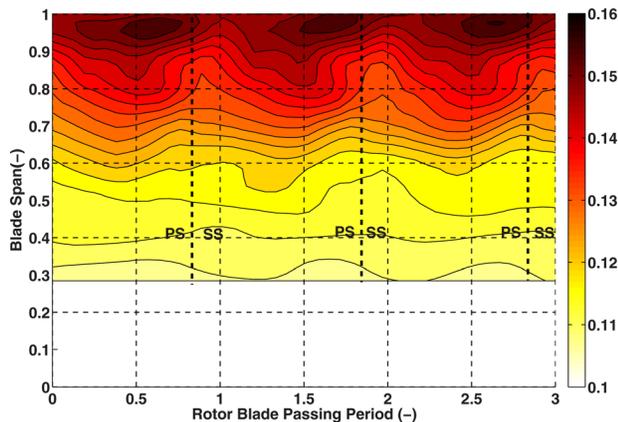
pressure fluctuations with Ref. [6]. As shown in Fig. 9(b), the highest values of RMS of P'_{tot} are located at 103% and 80% span for all conditions. Their origins will be further analyzed in the subsequent time-resolved results. At the midspan region, the small kink present at 50% span is linked to the presence of the PSC. Below 45% span, the RMS of P'_{tot} remains almost constant and gets its smallest value.

As indicated in Fig. 9(b), one can see that OP-3 shows higher values of stochastic unsteadiness at the tip region compared to OP-1 (maximum range of max–min values). At midspan, OP-3 shows an increase of 41% compared to OP-1. Below 40% span, the differences between the two conditions are relatively small. It is worth mentioning that there is more than a 50% change in RMS of P'_{tot} between the two conditions in the area above 100% span associated with the shroud leakage flow.

Similar observations can be made in Fig. 9(b) when OP-3 and OP-2 conditions are compared. The differences between the two conditions are in the same levels as the variations observed between OP-3 and OP-1, as described in the previous paragraph. However in this case, OP-2 shows higher stochastic unsteadiness in the region from 55% to 75% span, with 15% higher peak-to-peak variations in P'_{tot} compared to OP-1. This change might be related to the variations in the unsteady aerodynamic performance of the PSC among the different OPs.

Time-Resolved Flow Field at Rotor Exit of L-1 Stage. In order to further analyze the discrepancies of the flowfield along the blade span, the time-resolved data will now be discussed. As mentioned previously, the temporal resolution is limited to 16 measurement points for a rotor blade passage. Therefore, it is possible that very small flow features (i.e., blade wake) are resolved with limited samples. The corresponding time-resolved relative

(a)

Fig. 10 Time-resolved Cpt$_{rel}$ (——) at rotor exit of L-1 stage for OP-3

(b)
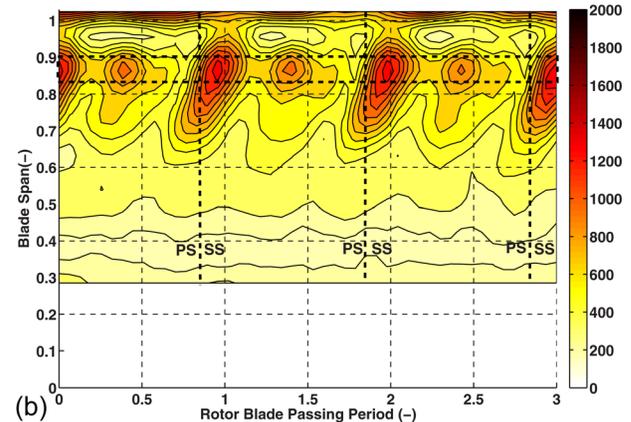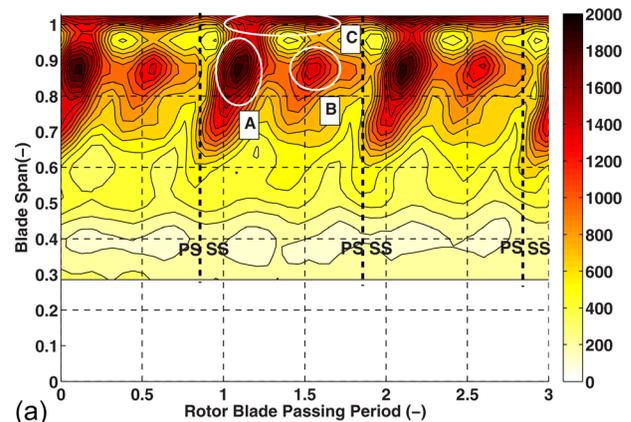
Fig. 11 Time-resolved RMS of P'_{tot} (Pa) in stationary frame of reference at rotor exit of L-1 stage for (a) OP-3 and (b) OP-1

(a)

(b)
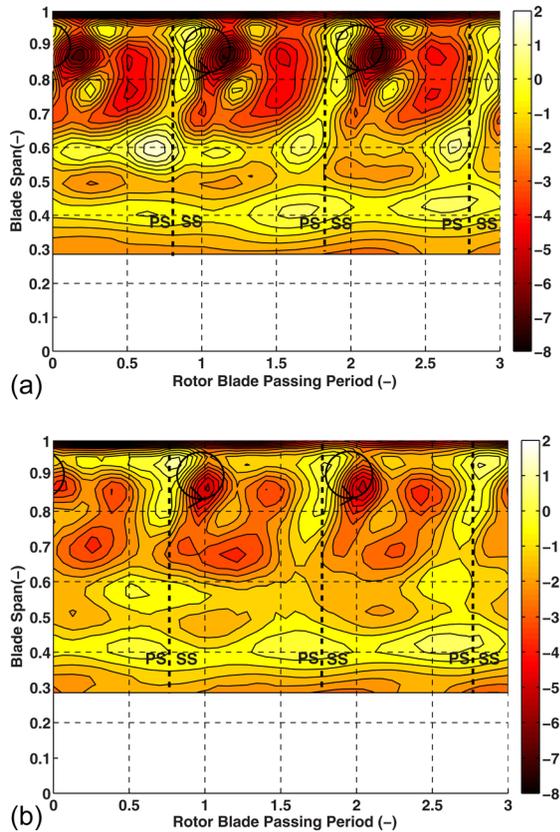
Fig. 12 Time-resolved relative yaw flow angle (deg) at rotor exit of L-1 stage for (a) OP-3 and (b) OP-1 (relative to blade metal angle)

total pressure coefficient for OP-3 is shown in Fig. 10. This is a space–time diagram for three consecutive blade passing events (phase lock averaged data) with the three dashed vertical lines representing the approximate position of the rotor blade trailing
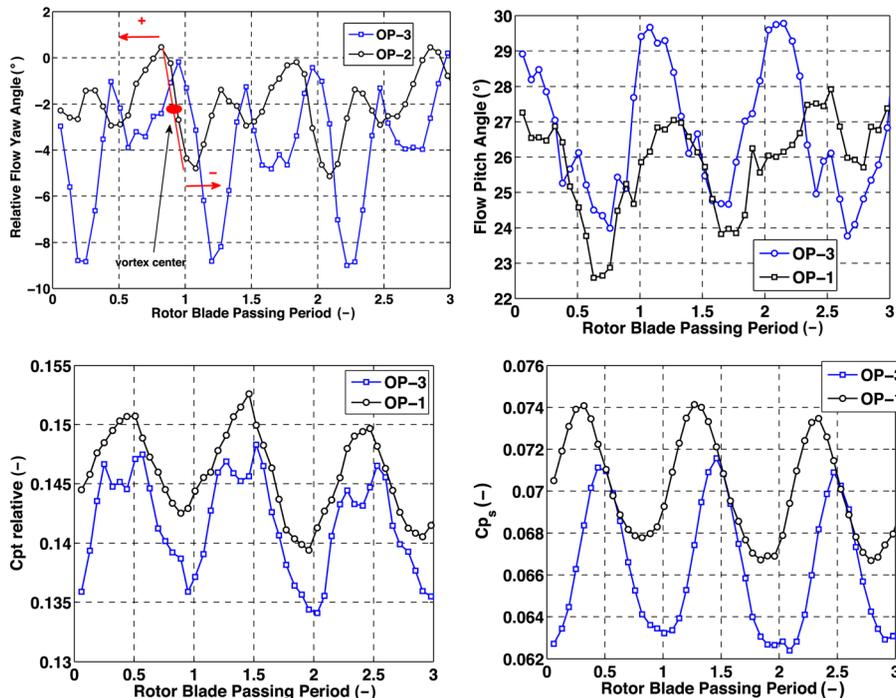
edges at $t/T = 0.75$, 1.75 and 2.75, respectively. The pressure side (PS) and suction side (SS) of each blade passage is indicated as well. The rotation is from left to right and the observer "looks" upstream. The measured total relative pressure variations are generally lowered adjacent to the hub and midspan relative to the tip. This is in good agreement with Fig. 9(b) and evidence that the flow field interaction with the rotor blades is predominant at the blade tip region (blade span > 65%).

In order to identify the secondary flow structures and assess their impact on the flow field among the different measured operating conditions, the unsteady results of the RMS of P'_{tot} are presented in Fig. 11. Due to the paper's space limitations, only the results of conditions OP-1 and OP-3 are analyzed. Three regions of elevated RMS of P'_{tot} can be identified over the measured blade span. The first are the regions A and B highlighted in Fig. 11(a) located at 90%, and occurring periodically at blade passing periods of $t/T = 0.1$, 1.1, and 2.1 and at $t/T = 0.6$, 1.6, and 2.6. The third region labeled as C is related to the tip labyrinth leakage flow and results in the highest values in the region of 103% span.

As presented in Fig. 11, it is believed that out of the two features located at 90% span, the one with the most elevated values (A) located on the SS of the rotor blade can be associated to the tip passage vortex. The second feature (B) is associated with the upstream stator's tip passage vortex. Similar secondary flow structure generated from the upstream stator, with lower intensity compared to the tip passage vortex, at 75% span, is reported by Chaluvadi et al. [25].

Figure 12 shows the respective time-resolved relative flow yaw angle at the rotor exit. In this graph, the relative flow yaw angle is subtracted from the blade metal angle in order to decouple the effect of the high twisting angle of the blade design. Positive values imply overturning, and negative values underturning. For this particular circumferential traverse location, the unsteady flowfield distribution is rather complex. It is most probably affected by the secondary flow structures generated in the two upstream stages. The tip passage vortex can be identified at the tip region at 90% span where the high alteration of the yaw angle (± 4.5 deg) is present in the SS at the rotor blade passing period of $t/T = 0.1$, 1.1, and 2.1. This vortex rotates counterclockwise as highlighted in Fig. 12(a). Since this region between 80% and 100% span is

Fig. 13 Unsteady relative flow yaw and pitch angles, relative total and static pressure coefficients at 86% span for OP-3 and OP-1
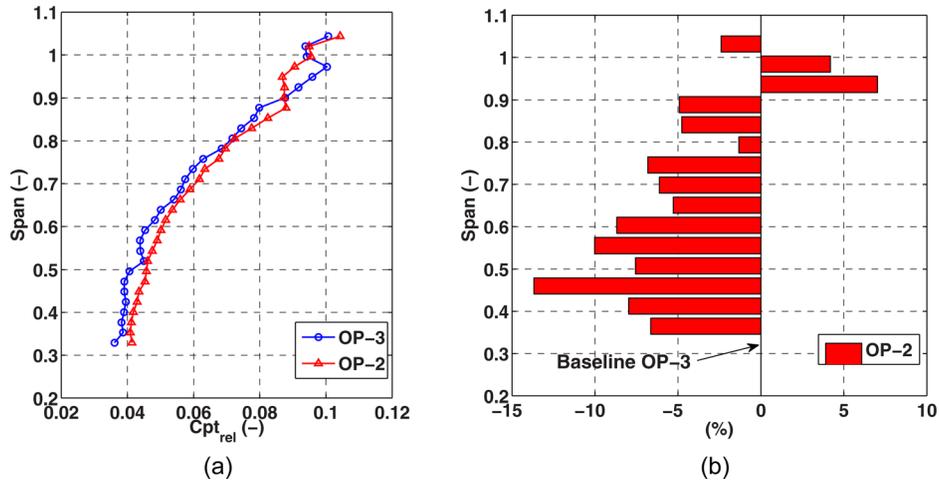
Fig. 14 Time-averaged spanwise distribution of the Cpt in relative frame of reference for two operating conditions (a) and difference in Cpt_{rel} between OP-2 with OP-3 (b)

dominated by secondary flow structures, the RMS of P'_{tot} (stochastic total pressure fluctuation) is maximum in the same location. This is confirmed in Fig. 11 where the highest values of P'_{tot} RMS are centered at 90% span on the SS of the rotor blade. Further evidences of the presence of the tip passage vortex are shown in Fig. 13, where the unsteady flow yaw angle, pitch angle, total pressure, and static pressure at 86% blade span are shown for OP-1 and OP-3 conditions for three rotor blade passing periods.

As previously described, the presence of the tip passage vortex at this spanwise location at the time instants $t/T = 0.1$, 1.1, and 2.1 results in variation of the yaw angle of ± 4.5 deg for OP-3 and ± 2 deg for OP-1, across the tip passage vortex. Accordingly, the pitch variation is ± 3 deg for OP-3 and ± 2 deg for OP-2. In Fig. 13, the peak-to-peak variation in relative total pressure is 14% of the average relative total pressure level for OP-3 and 11% for OP-1.
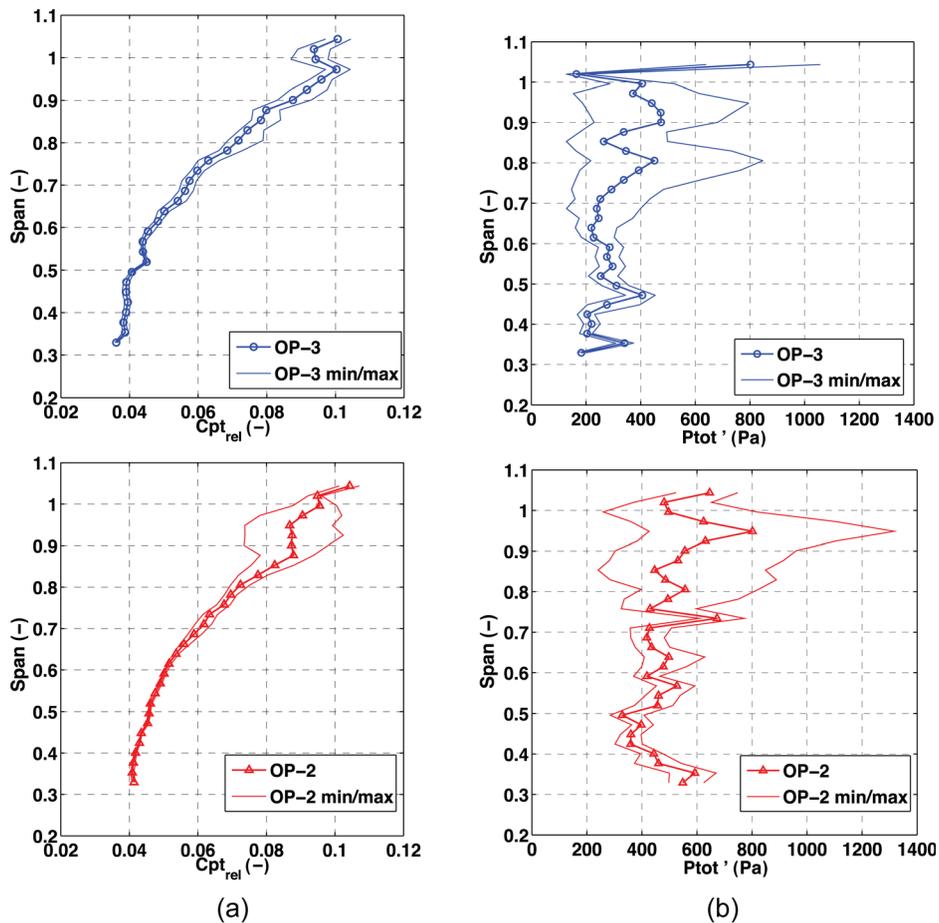
Fig. 15 Time-averaged spanwise distribution of Cpt_{rel} (a) and time-averaged P'_{tot} RMS (Pa) (b) at rotor exit of L-0 stage for OP-2 and OP-3 with their respective minimum and maximum values obtained from the time-resolved data
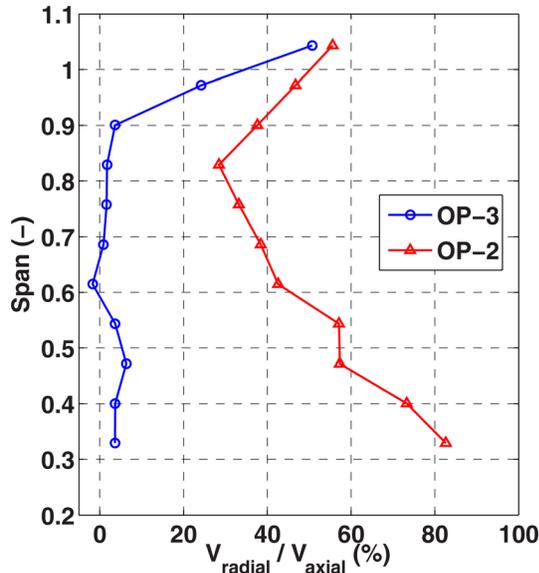
Fig. 16 Time-averaged spanwise distribution of V_{radial}/V_{axial} at exit of L-0 stage

One more observation worth noting is related to the presence of the PSC in Fig. 12. The snubber results in a small alternation of the yaw angle of ± 1 deg and its influence on the flow is $\pm 10\%$ in span from its design location (52% span). Häfele et al. [8] have reported similar values for the impact of the PSC downstream of the rotor blade in steam turbine measurements.

As shown in Fig. 12(a), the flow at the operating condition 3, in the region from 65% up to 100% span, exhibits higher underturning compared to the flow at OP-1. The result is that the secondary flow structures are more enhanced and therefore generate higher aerodynamic losses in that particular regime, as previously described in Fig. 9(b). This is in good agreement with the results in Fig. 11, where OP-1 creates 25% less P'_{tot} RMS in the structures A and B.

Steady Flow Field at Rotor Exit of L-0 Stage. In this paragraph, the time-averaged results of the FRAP-HTH probe at the exit of L-0 stage are presented for two different OPs for compactness of this paper. All plots show measurement results from 1.04 down to 0.33 span. Figure 14(a) depicts the time-averaged spanwise distribution of the relative pressure coefficient for OP-2 and OP-3 as described in Eq. (2). Condition OP-3 shows on an average 4.7% lower relative Cpt value and this can be attributed to the higher relative velocity across the span, which results in greater viscous losses. However, as shown in Fig. 14(b), an inversion of the aerodynamic losses is observed at 95% span, where OP-2 shows 5% greater losses compared to OP-3 for this measurement plane. The results in Fig. 14(b) are derived with the percentage Eq. (5) for each radial measurement point.

$$\frac{\overline{Cpt_{rel, \; OP-3}} - \overline{Cpt_{rel, \; OP-2}}}{\overline{Cpt_{rel, \; OP-3}}} \times 100 \qquad (5)$$

In order to understand the reason for this variation at the blade tip of the L-0 stage, the time-resolved peak-to-peak variations of Cpt_{rel} for OP-2 and OP-3 are shown in Fig. 15(a) together with their respective time-averaged distribution across the span. It can be seen that at the region of 95% span, the peak-peak fluctuations of the Cpt_{rel} are three times larger for OP-2, the condition with the reduced mass flow, compared to OP-3. The maximum peak to peak fluctuations are 33% of the mean value for OP-2 at 92% span. On the other hand below 80% span, as seen in Fig. 15(a),

both conditions show very similar and low unsteady relative total pressure behavior.

In Fig. 15(b), the RMS values of P'_{tot} are presented for OP-2 and OP-3. At 95% span, OP-2 gets the highest P'_{tot} RMS value, highlighting the presence of enhanced secondary flow structures compared to OP-3. This observation is in good agreement with Fig. 15(a) representing the region of high periodical unsteadiness at 92–95% span. The results of L-1 and L-0 stages for OP-2 and OP-3 contradict each other. The reason for this phenomenon is the sensitivity to the operating condition of the last stage in a steam turbine. In the current study, OP-2 operates with 22.4% reduced mass flow compared to OP-3.

As shown in Fig. 16, when the volume flow of the machine is reduced (OP-2), the fluid is redirected toward the tip region of the blade, which will strengthen the intensity of the three-dimensional turbulent flow structures present at the tip as shown in Figs. 15(a) and 15(b). This behavior has been confirmed by several experimental studies related to windage conducted in air or steam model test turbines [4,15,26].

Time-Resolved Flow Field at Rotor Exit of L-0 Stage. The time-resolved measurements performed at the rotor exit are presented in this paragraph for a single circumferential traverse. Figure 17 shows the spanwise distribution of the P'_{tot} RMS plotted over three consecutive blade passing events for OP-3 and OP-2. As seen in Figs. 17(a) and 17(b), the P'_{tot} RMS distribution across the span exhibits multiple cores of highly turbulent flow structures located between 75% and 95% span, which are most likely generated from the rotor as well as from upstream stator. However, the

(a)

(b)
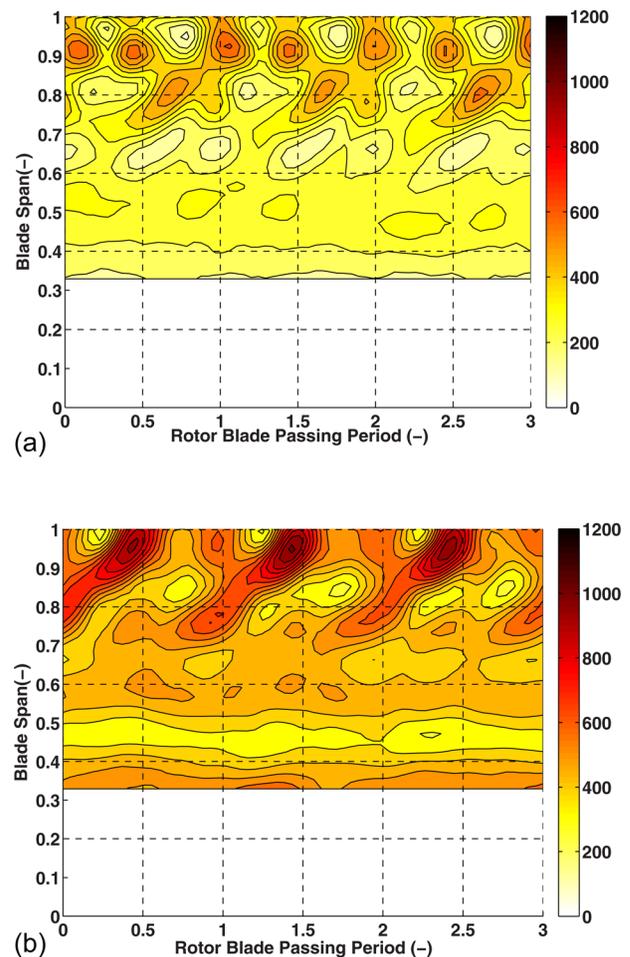
Fig. 17 Time-resolved RMS of P'_{tot} (Pa) in stationary frame of reference at rotor exit of L-0 stage for (a) OP-3 and (b) OP-2
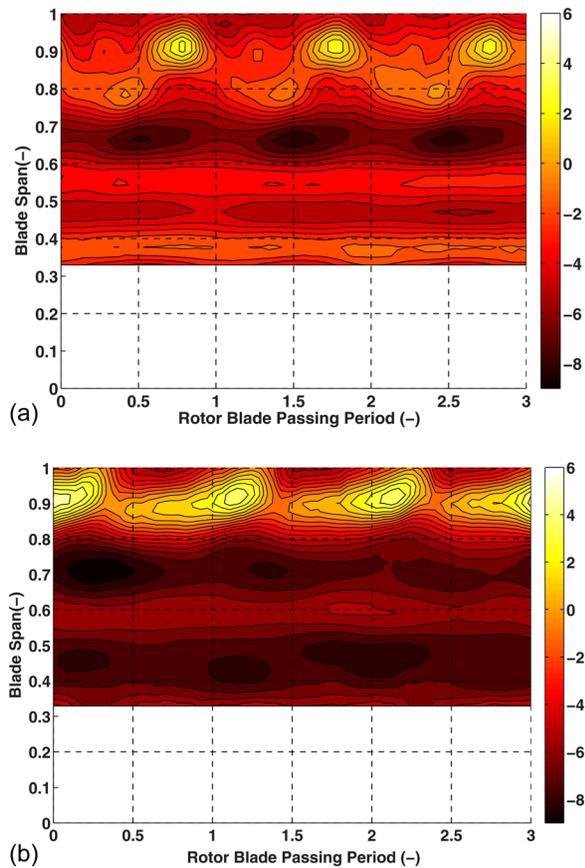
Fig. 18 Time-resolved relative flow yaw angle (deg) at rotor exit of L-0 stage for (*a*) OP-3 and (*b*) OP-2 (relative to blade metal angle)

Fig. 19 Time-resolved Cpt$_{rel}$ (—) at rotor exit for (*a*) OP-3 and (*b*) OP-2

single traverse type of measurement does not allow a clear identification of their origin. Nevertheless, one can identify that the high values of P'_{tot} RMS located between 80% and 95% span, for both operating conditions are driven periodically by the rotor blade passing period. OP-2 presented in Fig. 17(*b*) shows 60% higher values of P'_{tot} RMS compared to OP-3 for the turbulent structures located at 95% span, and 25% higher for the features located at 80% span.

Figure 18 shows the time-resolved relative flow yaw angle at the rotor exit for the conditions OP-2 and 3. In this figure, the relative flow yaw angle is subtracted from the blade metal angle. Positive values infer to flow overturning and negative values to flow underturning. As a general observation, the flow regions of high P'_{tot} RMS in Fig. 17, located between 80% and 95%, results in local flow underturning in Fig. 18, which is a typical signature of secondary flow structures. In Fig. 18, the peak-to-peak fluctuations of the relative flow yaw angle between 80% and 95% span is of ±4 deg for OP-3 and of ±5 deg for OP-2. The higher levels of relative yaw angle periodical unsteadiness found in OP-2 compared to OP-3 are in good agreement with the observed variations in P'_{tot} RMS between the two conditions. If we now extend the analysis to the Cpt$_{rel}$ temporal distribution, one can see that the magnitude of the observed periodical unsteadiness in Cpt$_{rel}$ presented in Figs. 19(*a*) and 19(*b*) are in line with the P'_{tot} RMS temporal and spatial distribution.

In Fig. 19(*a*), it can be seen that the peak-to-peak variation in Cpt$_{rel}$ at 92% span is 11% of the mean value for OP-3, whereas in Fig. 19(*b*) the peak-to-peak fluctuations at 92% span is 33% of the mean value for OP-2. Therefore, it can be concluded that due to the onset of the steam turbine ventilation process, condition OP-2 shows three times higher relative total pressure fluctuation at the region of 95% span compared to OP-3. This is also the reason for
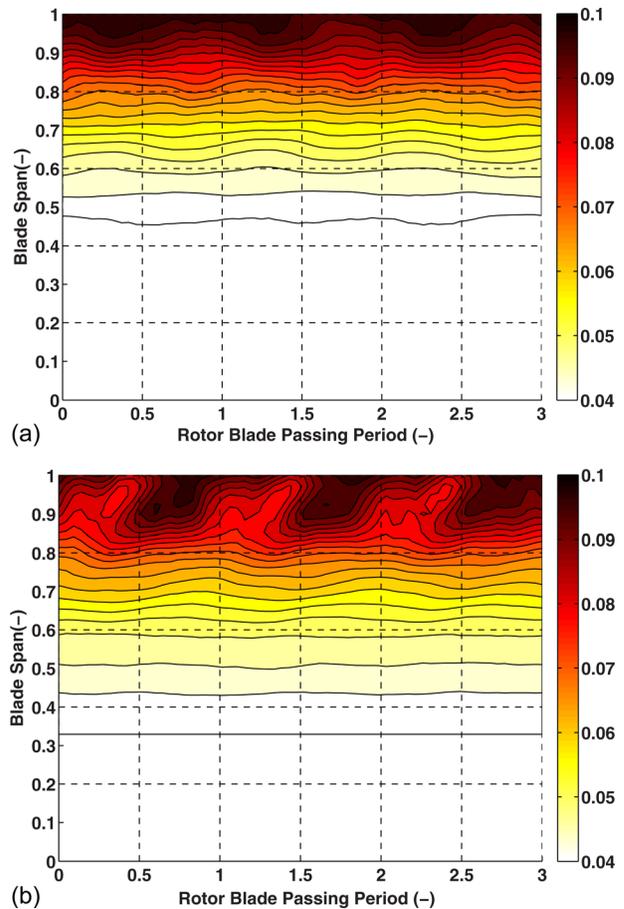
the 5% decrease in aerodynamic efficiency around the tip, as shown in Fig. 14(*b*).

Summary

A unique high temperature fast response probe for wet steam flow conditions has been developed and tested. The FRAP-HTH probe is based on the standard FRAP-HT probe. The FRAP-HTH probe is equipped with a miniature heater located in close vicinity to the tip of the probe. The heater allows the probe tip to be kept at a stable temperature above the flow saturation temperature and therefore keep the pressure taps unclogged. In this way the probe tip surface is clean from any water contamination. In addition, a virtual six-sensor probe measurement concept has been applied in order to allow measurements in flow regimes with high pitch angles up to 50 deg.

The FRAP-HTH measurements presented in the current paper were conducted at MHPS' research steam turbine test facility at the rotor exit of the last two stages under high and low massflow conditions. Good level of agreement in flowfield measurements was found between the FRAP-HTH and the commonly used 5HP for the most severe operating condition with high wetness mass fraction of 8% and absolute Mach number above Ma = 0.6. These measurements enabled a detailed analysis of the evolution of the secondary flow structures responsible for the unsteady aerodynamic loading of the blades.

Conclusions

- The novel fast response heated probe, demonstrated its reliability for accurate measurements in severe wet steam

conditions with wet-mass fractions up to 8% at the last stages of a steam turbine

- Measurements have shown that the heater which leads to an overheat of the probe tip has no effect on the measured flow quantities. The measured flow quantities with or without the heater activated are within the uncertainty of the aeromodel of the probe.
- The measurements have shown that the secondary flow structures at the tip region (shroud leakage and tip passage vortices) are the predominant sources of unsteadiness over the last 30% of the blade span for all operating conditions
- At the outlet of the last stage (L-1), the intensity of periodical fluctuations is found to be maximum for the high massflow condition (OP-3), with 8% fluctuation in relative total pressure.
- In contrast at the exit of the last stage, the reduced mass flow operating condition (OP-2) shows up to three times higher pressure fluctuations between 85% and 100% span as compared to OP-3, causing 5% higher aerodynamic losses. The reason for this phenomenon is the redirection of the flow towards the blade tip region resulting in the strengthening of the secondary flow structures.

Acknowledgment

Nomenclature

Cpt = total pressure coefficient
K = aerodynamic coefficient
P, p = pressure (Pa)
t = time instant
T = temperature (°C), time period
V = velocity (m/s)

Greek Symbols

γ = flow pitch angle (deg)
φ = flow yaw angle (deg)

Subscripts

dyn = dynamic
heater = heater location
rel = relative
s, stat = static
sat = saturation
t, tot = total
tip = probe tip location (sensors' region)

Superscripts

$\sim$ = time-resolved data (phase locked)
$\_$ = time-averaged data (mean value)
$'$ = random part of pressure signal

Abbreviations

FRAP-HTH = high temperature, fast response aerodynamic heated probe
MHPS = Mitsubishi Hitachi Power Systems
OP = operating point
PS = pressure side
PSC = part-span connector
RMS = root mean square
SS = suction side
5HP = pneumatic five-hole probe (Cobra shape)

References

[1] Senoo, S., and Ono, H., 2013, "Development of Design Method for Supersonic Turbine Aerofoils Near the Tip of Long Blades in Steam Turbines: Part 2—Configuration Details and Validation," ASME Paper No. GT2013-95827.

[2] Miller, R. J., Moss, R. W., Ainsworth, R. W., and Horwood, C. K., 2003, "Time-Resolved Vane–Rotor Interaction in a High-Pressure Turbine Stage," ASME J. Turbomach., 125(1), pp. 1–13.

[3] Hodson, H. P., and Dawes, W. N., 1998, "On the Interpretation of Measured Profile Losses in Unsteady—Turbine Blade Interaction Studies," ASME J. Turbomach., 120(2), pp. 276–284.

[4] Megerle, B., Stephen Rice, T., McBean, I., and Ott, P., 2012, "Numerical and Experimental Investigation of the Aerodynamic Excitation of a Model Low-Pressure Steam Turbine Stage Operating Under Low Volume Flow," ASME J. Eng. Gas Turbines Power, 135(1), p. 012602.

[5] Miyake, S., Koda, I., Yamamoto, S., Sasao, Y., Momma, K., Miyawaki, T., and Ooyama, H., 2014, "Unsteady Wake and Vortex Interactions in 3-D Steam Turbine Low Pressure Final Three Stages," ASME Paper No. GT2014-25491.

[6] Qi, M., Yang, J., Yang, R., and Yang, H., 2013, "Investigation on Loading Pulsation of LP Long Blade Stage in Steam Turbine," ASME Paper No. GT2013-94652.

[7] Sigg, R., Casey, M. V., Mayer, J. F., and Sürken, N., 2008, "The Influence of Lean and Sweep in a Low Pressure Steam Turbine: Analysis of Three Stages With a 3D CFD Model," ASME Paper No. GT2008-50161.

[8] Häfele, M., Starzmann, J., Grübel, M., Schatz, M., Vogt, D. M., Drozdowski, R., and Völker, L., 2014, "Numerical Investigation of the Impact of Part-Span Connectors on Aero-Thermodynamics in a Low Pressure Industrial Steam Turbine," ASME Paper No. GT2014-25177.

[9] Mistry, H., Santhanakrishnan, M., Liu, J., Stein, A., Dey, S., and Slepski, J., 2011, "Aerodynamic Performance Assessment of Part-Span Connector of Last Stage Bucket of Low Pressure Steam Turbine," ASME Paper No. POWER2011-55265.

[10] Völker, L., Casey, M., Dunham, J., and Stüer, H., 2008, "The Influence of Lean and Sweep in a Low Pressure Steam Turbine: Throughflow Modelling and Experimental Measurements," ASME Paper No. GT2008-50161.

[11] Parvizinia, M., Berlich, C., Truckenmüller, F., and Stüer, H., 2004, "Numerical and Experimental Investigations Into the Aerodynamic Performance of a Supersonic Turbine Blade Profile," ASME Paper No. GT2004-53823.

[12] Tsukuda, T., Sato, H., Nomura, D., Kawasaki, S., and Shibukawa, N., 2014, "An Experimental Investigation of Thermal Wetness Loss in the Full Scale Size Low Pressure Turbine," ASME Paper No. GT2014-26012.

[13] Cai, X., Ning, T., Niu, F., Wu, G., and Song, Y., 2009, "Investigation of Wet Steam Flow in a 300 MW Direct Air-Cooling Steam Turbine. Part 1: Measurement Principles, Probe, and Wetness," Proc. Inst. Mech. Eng., Part A, 223(5), pp. 625–634.

[14] Shibukawa, N., Iwasaki, Y., Takada, Y., Murakami, I., Suzuki, T., and Fukushima, T., 2014, "An Experimental Investigation of the Influence of Flash-Back Flow on Last Three Stages of Low Pressure Steam Turbines," ASME Paper No. GT2014-26897.

[15] Segawa, K., Senoo, S., Kudo, T., Nakamura, T., and Shibashita, N., 2012, "Steady and Unsteady Flow Measurements Under Low Load Conditions in a Low Pressure Model Steam Turbine," ASME Paper No. POWER2012-54862.

[16] Gerschütz, W., Casey, M., and Truckenmüller, F., 2005, "Experimental Investigations of Rotating Flow Instabilities in the Last Stage of a Low-Pressure Model Steam Turbine During Windage," Proc. Inst. Mech. Eng., Part A, 219(6), pp. 499–510.

[17] Kuperfschmied, P., Köppel, P., Roduner, C., and Gyarmathy, G., 2000, "On the Development and Application of the FRAP (Fast-Response Aerodynamic Probe) System for Turbomachines—Part 1: The Measurement System," ASME J. Turbomach., 122(3), pp. 505–516.

[18] Pfau, A., Schlienger, J., Kalfas, A. I., and Abhari, R. S., 2002, "Virtual Four Sensor Fast Response Aerodynamic Probe (FRAP)," 16th Symposioum on Measuring Techniques in Transonic and Supersonic Flow in Cascades and Turbomachines, Cambridge, UK, Sept. 23–24, Paper No. 5-1.

[19] Lenherr, C., Kalfas, A. I., and Abhari, R. S., 2010, "High Temperature Fast Response Aerodynamic Probe," ASME J. Eng. Gas Turbines Power, 133(1), p. 011603.

[20] Mansour, M., Kocer, G., Lenherr, C., Chokani, N., and Abhari, R. S., 2011, "Seven-Sensor Fast-Response Probe for Full-Scale Wind Turbine Flowfield Measurements," ASME J. Eng. Gas Turbines Power, 133(8), p. 081601.

[21] Bosdas, I., Mansour, M., Kalfas, A. I., and Abhari, R. S., "A Fast Response Miniature Probe for Wet Steam Flow Field Measurements," Meas. Sci. Technol. (submitted).

[22] Gallington, R. W., 1980, "Measurement of Very Large Flow Angles With Non-Nulling Seven-Hole Probe," Aeronautics Digest, Spring/Summer, Paper No. USAFA-TR-80-17, pp. 60–80.

[23] Behr, T., 2007, "Control of Rotor Tip Leakage and Secondary Flow by Casing Air Injection in Unshrouded Axial Turbine," DS dissertation, Swiss Federal Institute of Technology Zurich, Zurich, Switzerland, Paper No. ETH No. 17283.

[24] Porreca, L., Hollenstein, M., Kalfas, A. I., and Abhari, R. S., 2007, "Turbulence Measurements and Analysis in a Multistage Axial Turbine," J. Propul. Power, 23(1), pp. 227–234.

[25] Chaluvadi, V. S. P., Kalfas, A. I., Banieghbal, M. R., Hodson, H. P., and Denton, J. D., 2001, "Blade-Row Interaction in a High-Pressure Turbine," J. Propul. Power, 17(4), pp. 892–901.

[26] Sigg, R., Heinz, C., Casey, M. V., and Sürken, N., 2009, "Numerical and Experimental Investigation of a Low-Pressure Steam Turbine During Windage," J. Power Energy, 223(6), pp. 697–708.